Porous 2D Catalyst Covers Improve Photoelectrochemical Water-oxidation Performance

Guancai Xie, Xiaolong Liu, Beidou Guo, Ting Tan, and Jian Ru Gong**

G. Xie, B. Guo, J. R. Gong

Chinese Academy of Sciences (CAS) Center for Excellence in Nanoscience, CAS Key Laboratory for Nanosystem and Hierarchical Fabrication, National Center for Nanoscience and Technology, Beijing 100190, China

E-mail: gongjr@nanoctr.cn

X. Liu, T. Tan

Laboratory of Theoretical and Computational Nanoscience, CAS Key Laboratory of Nanophotonic Materials and Devices, National Center for Nanoscience and Technology, Beijing 100190, China

E-mail: tant@nanoctr.cn

T. Tan, J. R. Gong

University of CAS, Beijing 100049, China

Keywords: 2D-covered catalyst, porous graphene, photoelectrochemical water oxidation

This article has been accepted for publication and undergone full peer review but has not been through the copyediting, typesetting, pagination and proofreading process, which may lead to differences between this version and the Version of Record. Please cite this article as doi: 10.1002/adma.202211008.

Confined catalysis under the cover of two-dimensional (2D) materials has emerged as a promising approach for achieving highly effective catalysts in various essential reactions. Here, a porous cover structure is designed to boost the interfacial charge and mass transfer kinetics of 2D-covered catalysts. The improvement in catalytic performance is confirmed by the photoelectrochemical oxidation evolution reaction (OER) on a photoanode based on an n-Si substrate modified with a NiO_x thin-film model electrocatalyst covered with a porous graphene (pGr) monolayer. Experimental results demonstrate that the pGr cover enhances the OER kinetics by balancing the charge and mass transfer at the photoanode and electrolyte interface compared to the intrinsic graphene cover and cover-free control samples. Theoretical investigations further corroborate that the pore edges of the pGr cover boost the intrinsic catalytic activity of active sites on NiO_x by reducing the reaction overpotential. Furthermore, the optimized pores, which can be easily controlled by plasma bombardment, allow oxygen molecules produced in the OER to pass through without peeling off the pGr cover, thus ensuring the structural stability of the catalyst. This study highlights the significant role of the porous cover structure in 2D-covered catalysts and provides new insight into the design of high-performance catalysts.

1. Introduction

As a new type of confined catalysis, circumscribing catalytic reactions under a two-dimensional (2D) cover has emerged as a viable strategy for achieving potent and efficient catalysts in various important reactions.[1-4] The confinement effect in 2D-covered catalysts was first demonstrated in low-pressure CO catalytic oxidation experiments.[3,5] Later, theoretical reports revealed that metal or metal oxide with 2D covers could promote H_2 evolution[6,7] and CO_2 reduction reactions[8,9]. These 2D covers have been found either to reduce the adsorption free energy of reactants on the catalyst surface or to improve charge transfer efficiency, leading to enhanced catalytic reactivity.[2,6,7,9-11]

As the archetypal 2D material, graphene (Gr) is per se electrochemically inert and can be grown or transferred on substrates of different nature, making it an ideal theoretical model for the studying of 2D-covered catalysis. However, Gr poses a very high energy barrier (at least several electronvolts) for penetration of atoms and molecules, which will prohibit any gas and liquid permeation under ambient conditions in principle.[12] Fu et al. provided experimental evidence that only hydrions (H^+) could reversibly penetrate the monolayer Gr cover on the Pt(111) surface and be electrochemically reduced to adatoms, while other bulky cations and anions were completely blocked under the electrochemical environment.[13] A recent experiment work by Koper et al. proved that Gr blocks the interaction of anions with the underlying Pt(111) catalyst surfaces, and proton permeation in the Gr layer occurs via the domain boundary and point defects.[14] It can be inferred that the Gr cover will restrict access of reactant ions/molecules to the underlying confined catalytic surface and prohibit the release of products from the confined zone. This not only limits the charge and mass transfer in the catalytic reactions but also leads to possible structural damage of the confined zone due to the build-up of pressure from the gas products.[1] Although intrinsic defects such as vacancies or grain boundaries have been present in the early confined catalysts,[2,3] however, the corresponding theoretical studies were based on the ideal models with perfect structures of 2D covers, which might cause some discrepancies from actual cases in explaining the catalytic mechanism.

Density functional theory (DFT) calculations suggest that structural defects in Gr are crucial in altering the interaction of adsorbates with catalysts in 2D confined spaces or changing the electrocatalytic active sites in 0D Gr or carbon shell covered particle electrocatalysts.[1,5,10,15,16] Recent experiments have demonstrated that the electrocatalytic H_2 production activity of the 2D-covered catalysts can be modified by changing the 2D cover structure, such as doping, defects, and layer numbers, owing to the accordingly tuned proton penetration degree.[17-19] However, their investigations have been only focused on the mass transfer process of reactions.[17,19] For instance, Hu et al. studied the influence of proton penetration through Gr layers on the electrocatalytic hydrogen evolution mechanisms of Ni and Cu in an acidic electrolyte.[17] They found that the degree of proton penetration, as determined by the number of Gr-covering layers, dominates the electrocatalytic activity of Gr-covered catalysts. Nevertheless, a rational structural design of 2D covers to tailor both intrinsic catalytic nature and charge and mass transfer is highly desirable for high-performance 2D-covered catalysts.

Here, we designed a novel porous cover structure to improve the performance of 2D-covered catalysts. The photoelectrochemical (PEC) water oxidation improvement was confirmed in the Si-based photoanode modified with a porous graphene (pGr) monolayer-covered NiO_x thin-film model electrocatalyst. The main reasons for choosing this PEC system are: (1) NiO_x thin film electrocatalysts have been well studied as surface modification in Si-based photoanodes;[20,21] (2) the atomically flat surface of the 2D Gr cover is convenient to integrate with the NiO_x thin film on the photoelectrode; (3) the low light absorption and scattering properties of the Gr monolayer can decrease light loss irradiated on the photoanode; and (4) the porous structure of Gr holds great potential to facilitate charge and mass transfer at the interface and avoid peeling off of Gr caused by the pressure build-up from gas products. This work aims to unveil the catalytic nature of 2D-covered catalyst by designing a porous cover structure from both experimental investigations and theoretical calculations. We found that the significantly improved performance is due to the optimal porous structure of the pGr cover facilely controlled by plasma bombardment, compared to the control sample with a pristine Gr cover. The resulting structure balances the interfacial charge and mass transfer, ensures the structural stability of the photoanode, and enhances the intrinsic catalytic activity of active sites on NiO_x. Our study sheds light on the new understanding of catalytic reactions under 2D covers from the aspect of intrinsic catalytic properties. It offers a new design strategy for high-performance PEC devices. Our findings can be further extended to other 2D-covered catalyst systems, broadening their potential applications.

2. Results and Discussion

2.1. Preparation and characterization of photoanodes

The procedure of fabricating photoanodes is depicted in **Figure 1**a. First, an n-Si substrate was used as the light absorber of the photoanode after cleaning, owing to its appropriate bandgap (1.1 eV) and excellent charge transport properties (step 1). Next, the TiO_2 thin layer (~2 nm) was obtained by atomic layer deposition (ALD) to serve as the tunneling dielectric layer that passivates surface states on the n-Si surface (step 2).[22] Then, the Ni layer with a thickness of 4 nm was deposited through thermal evaporation. It provides adequate protection against corrosion to n-Si while maintaining favorable PEC oxygen evolution reaction (OER) activity (step 3).[22] Subsequently, the chemical vapor deposited Gr monolayer (Figure S1, Supporting Information) was transferred onto the n-Si/TiO_2/Ni substrate (step 4). A porous structure in the Gr monolayer (pGr) was created with Ar plasma bombardment. The sample was baked in ambient conditions to transform the Ni layer into a NiO_x phase, which enhanced the adhesion of the pGr on the substrate, resulting in the final n-Si/TiO_2/NiO_x/pGr photoanode (step 5). In comparison, the n-Si/TiO_2/NiO_x/Gr with the pristine Gr cover was obtained as a control sample without plasma bombardment while keeping other steps the same as the n-Si/TiO_2/NiO_x/pGr. And the Gr-free n-Si/TiO_2/NiO_x photoanode was also prepared as a blank control.

To characterize the surface morphology of the as-prepared photoanodes, scanning electronic microscopy (SEM) was employed. The typical SEM image of the n-Si/TiO_2/NiO_x/pGr sample (with the bombardment time of 15s here and hereafter unless otherwise specified) displays that the pGr sheet completely covers the surface of the photoanode (Figure S2a, Supporting Information), which is similar to that of the n-Si/TiO_2/NiO_x/Gr (Figure S2b, Supporting Information). The n-Si/TiO_2/NiO_x displays a planar structure free of any sheets (Figure S2c, Supporting Information), and most parts of the Gr and pGr sheets are single atomic layers. Therefore, both n-Si/TiO_2/NiO_x/pGr and n-Si/TiO_2/NiO_x/Gr samples should exhibit a flat surface morphology.

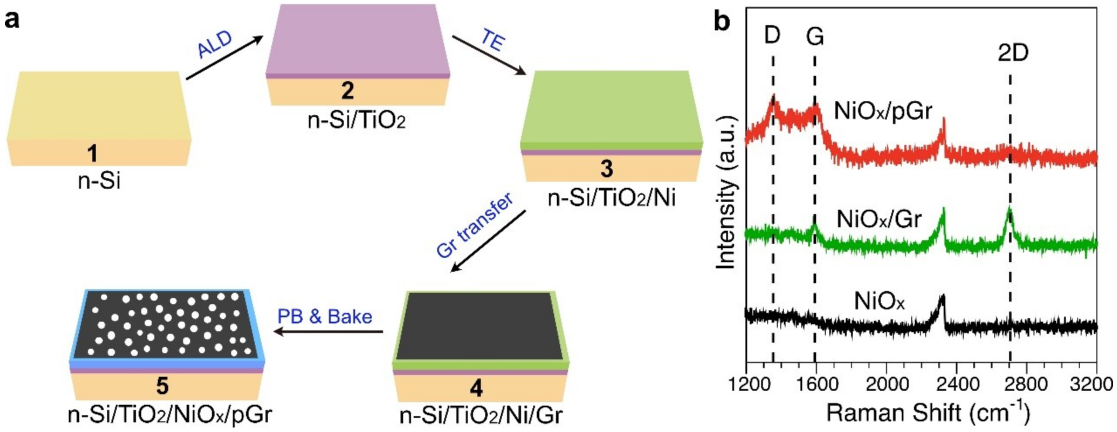

Figure 1. (a) Schematic diagram of the procedure for fabricating the n-Si/TiO_2/NiO_x/pGr photoanode. ALD, TE, and PB represent atomic layer deposition, thermal evaporation, and plasma bombardment, respectively. (b) Raman spectra for the n-Si/TiO_2/NiO_x/pGr (red), n-Si/TiO_2/NiO_x/Gr (green), and n-Si/TiO_2/NiO_x (black) photoanodes, denoted as NiO_x/pGr, NiO_x/Gr, and NiO_x, respectively for clarity in the figures here and hereafter unless otherwise specified.

Raman spectroscopy was used to further investigate the 2D cover structure on the photoanode surface.[23] The Raman spectrum of the n-Si/TiO_2/NiO_x/Gr sample clearly displays the characteristic G and 2D peaks of Gr, which are located at around 1600 and 2700 cm^{-1}, respectively. And the unobservable defect-activated D peak at ~1360 cm^{-1} demonstrates the near-perfect honeycomb structure of the Gr cover;[23,24] while the Raman spectrum of the n-Si/TiO_2/NiO_x does not exhibit any characteristic Gr peaks as expected. In contrast, the Raman spectrum of the n-Si/TiO_2/NiO_x/pGr shows broad D and G peaks and the disappearance of the 2D peak, suggesting the formation of a porous structure in the pGr cover.

X-ray photoelectron spectroscopy (XPS) was then utilized to clarify the chemical composition of the photoanodes. The Ni 2p XPS spectrum of the n-Si/TiO_2/NiO_x/pGr photoanode is presented in **Figure 2**a and can be deconvoluted into six peaks, including two spin-orbit doublets and two shakeup satellites of Ni $2p_{3/2}$ and Ni $2p_{1/2}$. The spin-orbit doublet of Ni $2p_{3/2}$ and Ni $2p_{1/2}$, centered at 871.7 and 854.1 eV, respectively, is assigned to Ni^{2+}, and the other spin-orbit doublet at 873.5 and 855.9 eV corresponds to Ni^{3+}.[22,25,26] This XPS feature suggests that the original Ni film was fully converted to NiO_x with the Ni^{2+} and Ni^{3+} chemical states after baking treatment of the n-Si/TiO_2/Ni/pGr. The Ni 2p spectrum of the n-

Si/TiO_2/NiO_x exhibits a similar pattern as the n-Si/TiO_2/NiO_x/pGr. By contrast, the Ni^0 chemical state is observed in the n-Si/TiO_2/NiO_x/Gr with the spin-orbit doublet of Ni $2p_{3/2}$ and Ni $2p_{1/2}$ at 870.6 and 852.9 eV.[25,27] The presence of metallic Ni is attributed to the metal oxidation barrier of Gr, which slows oxygen diffusion in the air to the Ni layer.[28,29] The undetectable Ni^0 state in the n-Si/TiO_2/NiO_x/pGr suggests that the porous Gr structure is permeable easily for O_2 molecules to oxidize the Ni to NiO_x. This further validates the existence of the porous structure in the pGr, as concluded from the above Raman results. The deconvoluted C 1s peaks in Figure 2b and 2c show four binding energies of 284.8, 285.7, 286.7, and 289.1 eV, corresponding to double C=C (sp^2) and single C-C (sp^3) bonds in aromatic rings, C-O bonds, and C=O bonds, respectively.[30-32] The percentage of sp^3 C-C in the pGr (12.4%) is higher than that in the Gr (7.4%) due to the higher degree of disorder caused by the plasma bombardment. However, the percentage of sp^2 C=C bonds remains at 56.1%, suggesting that the pGr sheet is partly disordered with a roughly low sp^3 amorphous graphene structure. XPS data also reveal that the pGr cover has a significantly higher percentage of C=O and C−O bonding than the Gr cover. These hydrophilic groups in the pGr could become active sites for adsorption and activation of the reactive species in the electrolyte on the NiO_x surface.[33,34]

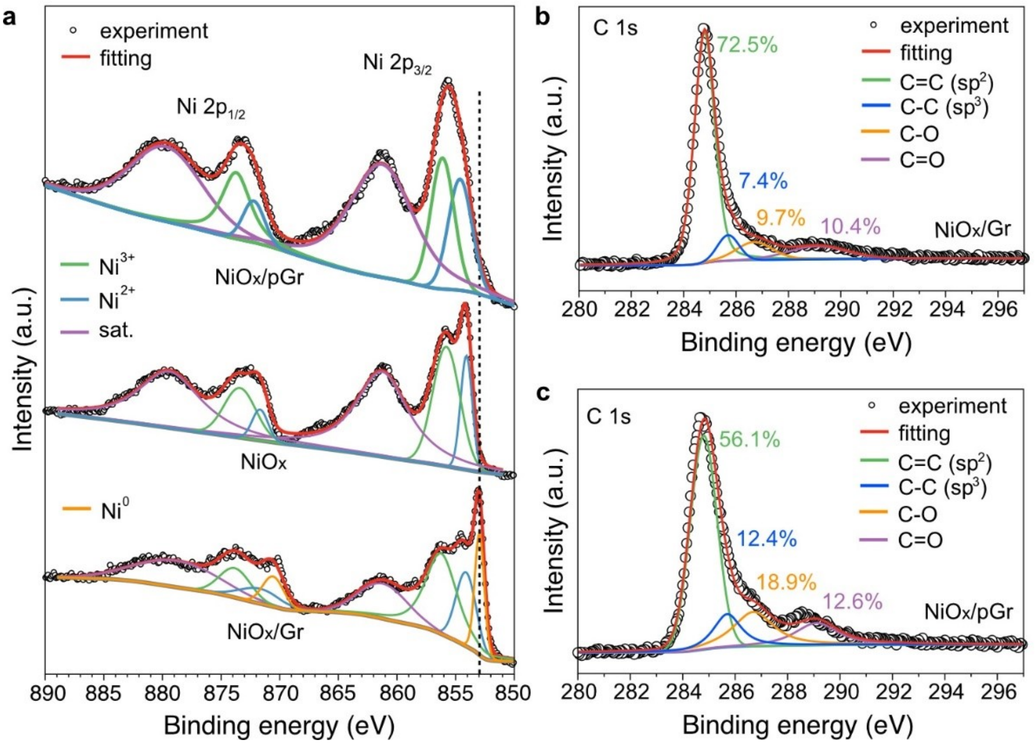

Figure 2. (a) High-resolution XPS spectra of Ni 2p for the n-Si/TiO_2/NiO_x/pGr, n-Si/TiO_2/NiO_x/Gr, and n-Si/TiO_2/NiO_x photoanodes. High-resolution XPS spectra of C 1s for the (b) n-Si/TiO_2/NiO_x/Gr and (c) n-Si/TiO_2/NiO_x/pGr photoanodes.

Furthermore, the pore size of the pGr cover can be tailored in a controllable manner by adjusting the plasma bombardment time. The two-stage model has been widely used to analyze the microscopic structural properties of graphene under ion bombardment.[35,36] In the first stage (Stage 1), crystalline graphene transforms into nanocrystalline form. In the second stage (Stage 2), nanocrystalline graphene changes to amorphous carbon. This can be further classified into two more specific regimes: nanocrystalline graphene-low sp^3 amorphous graphene and high sp^3 amorphous carbon.[37]

The structural evolution of the pGr with different plasma bombardment time was monitored by Raman spectroscopy. Herein, the 300-nm SiO_2/Si substrate instead of the n-Si was used on account of its high signal-to-noise ratio for the Raman test of graphene.[38] The results presented in **Figure 3**a reveal that: (1) the defect-activated D peak initially experiences a significant increase within the first 3 s, after which it decreases with prolonged bombardment time; (2) the D' peak, another signature of graphene disorder at ~1620 cm^{-1}, emerges at the 1s and mounts gradually until eventually merges with the G peak; (3) the G peak, arising from the E_{2g} vibrational mode found in the sp^2-bonded ordered graphitic carbon,[36] weakens in intensity and broadens as the bombardment time increases, which corresponds to the increasing full width at half maximum (FWHM) values as signified in Figure 3b; and (4) the 2D peak, associated with the breathing modes of six-atom rings,[36] progressively decreases until it nearly disappears.

The degree of the structural disorder in the pGr can be qualitatively estimated from the integrated intensity ratio of the D and G peaks (I_D/I_G), with a higher value indicating higher defect density in the system. Figure 3b shows that the I_D/I_G ratio surges with increasing bombardment time (≤ 3 s) and then drops (> 3 s) after reaching its maximum value. Therefore, the state at 3 s is taken as a boundary between Stage 1 and Stage 2.[37] The defect density in pGr can be quantified by determining the average distance between two adjacent defects (L_D), which can be estimated using the Tuinstra-Koening and Ferrari-Robertson relations for both stages (see Supplementary Note 1, Supporting Information).[39] The resulting plot of the I_D/I_G ratio as a function of the calculated L_D is presented in Figure 3c. According to the structural model[39] proposed by Lucchese *et al.* for the ion-bombarded graphene, the radii of structurally activated (r_A) and disordered (r_S) regions resulting from the impact of one Ar plasmonic ion are estimated to be 2.9 and 1.0 nm (Figure 3d), respectively, via fitting the experimental I_D/I_G values (See Supplementary Note 2, Supporting Information).[36,39,40] In the structurally activated region, the graphene lattice structure is preserved. However, the proximity to a defect results in a mixing of Bloch states near the K and K' valleys of the graphene Brillouin zone, thus breaking selection rules and enhancing the D band.[36,41] That is, the activated regions contribute strongly to the D band as compared to the structurally disordered regions. Therefore, as the number of impacts increases due to the bombardment time increasing, the pristine graphene sheet evolves to be mostly activated, leading to an increase in the D band. However, at Stage 2, the most structurally disordered regions become increasingly widespread, resulting in a decrease in the D band for longer bombardment time.[41] The $I_D/I_{D'}$ ratio is also used to probe the type of defects in graphene, where a value smaller than 7 corresponds to predominantly vacancy-type defects.[42,43] It thus suggests that the pores in the Gr sheet start to generate at a bombardment time longer than 1s (see details in Figure S3(a-d), Supporting Information).

At Stage 2, the structurally disordered regions become accumulatively widespread via overlapping neighboring ones,[44] ultimately transformed into complete amorphous carbon with an I_D/I_G ratio close to zero and the *sp*^{3} carbon reaching 20% according to Ferrari's model.[45] Combining the Raman analysis with above XPS results, it can be concluded that the pGr cover with an I_D/I_G value of 1.03 and a *sp*^{3} carbon ratio of 12.4 % under our condition, is close to a low *sp*^{3} amorphous graphene, as illustrated in Figure S4 (Supporting Information). The calculated defect density, n_D (cm^{-2}) = $10^{14}/(\pi L_D^2)$,[23] as a function of bombardment time is displayed in Figure S3e. The vacancy-type defects increase sharply at the beginning of Stage 1, reaching up to 10^{13} cm^{-2} by the end of this stage and remaining at this level during Stage 2. This suggests that the pores in the pGr sheet are mainly generated at Stage 1, and longer bombardment times (> 3 s) at Stage 2 lead to increased pore size by merging adjacent smaller pores.

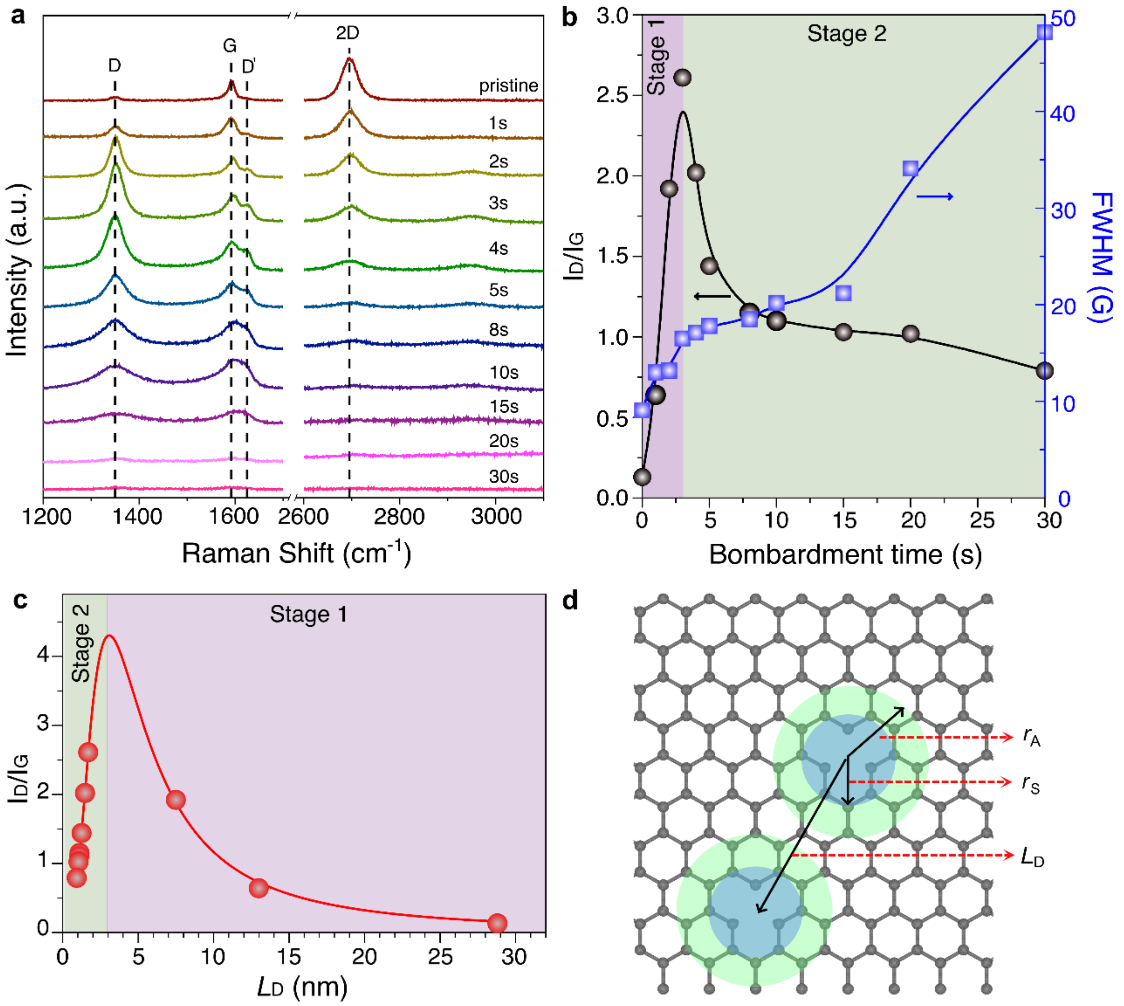

Figure 3. (a) Representative Raman spectra of the pGr sheet on the 300 nm-SiO_2/Si substrate at different Ar plasma bombardment time and that of the pristine Gr for comparison. (b) The I_D/I_G value and FWHM of the G peak as a function of plasma bombardment time, respectively. The solid curves are guides to the eye. (c) The I_D/I_G value as a function of L_D. The red curve is the theoretical modeling data. (d) The structural model of the pGr after the bombardment of one Ar plasmonic ion at Stage 1; r_A and r_S are the radii of structurally activated and disordered region, and L_D represents the average distance between two adjacent defects.

The structure evolution of pGr with respect to the bombardment time was further examined using transmittance electronic microscopy (TEM). **Figure 4** displays TEM images of three representative samples bombarded for 5, 15, and 30 s, respectively. No discernible pores are observed in the 5 s-bombarded sample (Figure 4a). However, as the bombardment time increases, pores with an average diameter of 3.56 nm are present in the 15 s-bombarded pGr sheet (Figure 4b, and Figure S5a, Supporting Information). With 30 s bombardment, the pore sizes are further increased to several dozen nanometers (with an average size of 14.37 nm) and even larger than 100 nm (Figure

4c, and Figure S5b, Supporting Information). This structure evolution detected by TEM is aligned with the above Raman analysis, demonstrating the growth in pore size of the pGr sheet with a longer bombardment time.

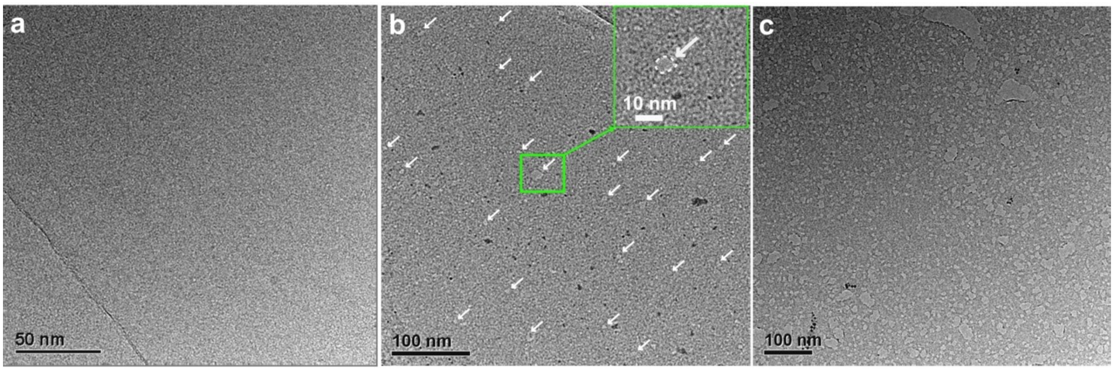

Figure 4. TEM images of the pGr samples after (a) 5, (b) 15, and (c) 30 s bombardment with Ar plasma.

2.2. PEC performance of photoanodes

The PEC water oxidation activity of the photoanodes was evaluated by performing linear sweep voltammetry measurements in 1 M KOH solution under simulated solar irradiation without correction for resistance loss in the electrolyte solution. The measured current density-potential (*J*-*V*) curves in **Figure 5**a depict that the bombardment time of the porous Gr significantly influences the PEC OER activity. Specifically, as the bombardment time increases, the OER activity of the photoanode first enhances up to the highest activity at the bombardment time of 15 s, corresponding to the pore diameter of 3–10 nm. Afterward, the OER activity gradually decreases with a longer bombardment time. As shown in Figure 5b, the n-Si/TiO_2/NiO_x/pGr photoanode yields a photocurrent onset potential (V_{on}, defined as the applied bias to get the photocurrent of 1 mA cm^{-2}) of 1.13 ± 0.01 V vs reversible hydrogen electrode (V_{RHE}) and a photocurrent density at 1.23 V_{RHE} ($J_{1.23}$) of 8.08 ± 1.0 mA cm^{-2}; while the n-Si/TiO_2/NiO_x/Gr only possesses a V_{on} of 1.19 ± 0.01 V_{RHE} and a $J_{1.23}$ of 2.40 ± 0.36 mA cm^{-2}, even worse than the V_{on} of 1.16 ± 0.02 V_{RHE} and a $J_{1.23}$ of 4.00 ± 0.77 mA cm^{-2} for the Gr-free n-Si/TiO_2/NiO_x (see Figure S6 for details, Supporting Information). Among the three photoanodes, the n-Si/TiO_2/NiO_x/pGr possesses the best PEC OER activity, and the n-Si/TiO_2/NiO_x/Gr is the worst, leaving the Gr-free n-Si/TiO_2/NiO_x at the median level. The dark current was measured to be close to zero over the potential applied in this test, confirming that the observed current under irradiation is correlated to the photogenerated charge carriers. Furthermore, the Faradaic efficiency of oxygen gas evolution for the n-Si/TiO_2/NiO_x/pGr photoanode (Figure S7, Supporting Information) was calculated. The efficiency fluctuated around 83% during the PEC reaction and finally reached 90.1% by detaching the O_2 bubbles that remained on the photoanode surface after the PEC reaction. This observation could be due to the back reaction of the dissolved oxygen and oxidation of Ni-based catalysts.[46] The characteristic D and G Raman peaks of pGr were still present for the n-Si/TiO_2/NiO_x/pGr photoanode even after the PEC measurement (Figure S8, Supporting Information), thus consolidates that the enhanced photocurrent mainly resulted from water oxidation rather than the oxidation of graphene. To ensure the reproducibility of the results and exclude the effects of unavoidable tears in the Gr and pGr covers, at least four independent experiments were conducted for each photoanode. It is thus clear that the porous Gr cover increases the PEC OER activity while the pristine Gr deteriorates it, compared to the cover-free photoanode.

To assess the PEC OER stability of the n-Si/TiO_2/NiO_x/pGr photoanode, chronoamperometric data were collected at a constant bias of 1.23 V_{RHE} in the 1 M KOH solution under simulated solar irradiation (Figure S9a, Supporting Information). The n-Si/TiO_2/NiO_x/pGr photoanode exhibited a 50% decrease in photocurrent density after the 12 h stability test, which could be attributed to the accumulation of oxygen bubbles on the surface that suppressed the OER reaction. After drying the surface using N_2 gas and changing to a new 1 M KOH solution, the photocurrent density of the n-Si/TiO_2/NiO_x/pGr photoanode was able to recover to the initial value, indicating the good photostability of the photoanode. Moreover, the *J-V* characteristics recorded after the 12 h durability test indicate that the n-Si/TiO_2/NiO_x/pGr photoanode can retain 90.1% of its initial photocurrent at 1.23 V_{RHE}, whereas the n-Si/TiO_2/NiO_x photoanode can retain only 51.7% of its initial value (Figure S9b, Supporting Information). Even after a 16 h durability test, the n-Si/TiO_2/NiO_x/pGr photoanode can still retain 76.6% of its initial photocurrent at 1.23 V_{RHE}, which further confirms the good stability of the n-Si/TiO_2/NiO_x/pGr photoanode compared to the n-Si/TiO_2/NiO_x control photoanode.

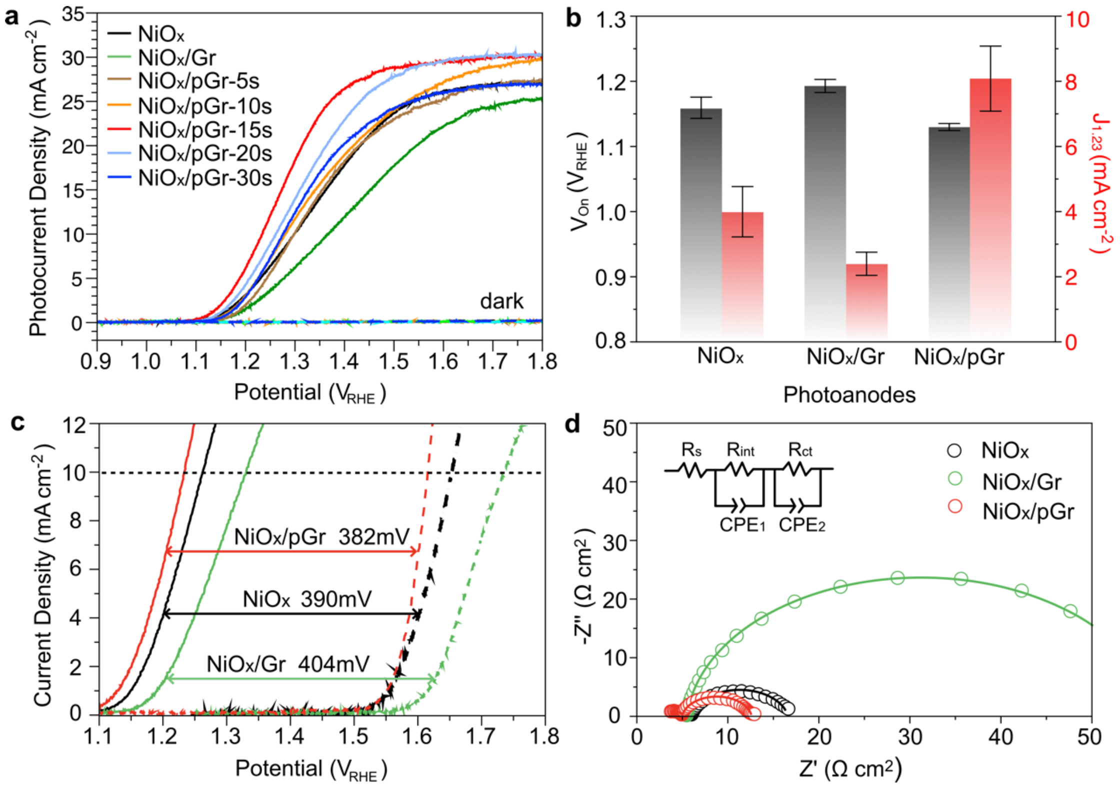

Figure 5. (a) Current density-potential (*J*-*V*) curves of the n-Si/TiO_2/NiO_x/pGr photoanode at different bombardment time measured in 1 M KOH aqueous solution without iR-compensation under AM 1.5G sunlight (100 mW cm^{-2}), and those of the n-Si/TiO_2/NiO_x/Gr and n-Si/TiO_2/NiO_x for comparison. (b) The V_{on} and $J_{1.23}$ values for the n-Si/TiO_2/NiO_x/pGr, n-Si/TiO_2/NiO_x/Gr, and n-Si/TiO_2/NiO_x photoanodes. The error bars correspond to the standard deviations of the multiple measurements. (c) Representative OER polarization plots in 1 M KOH for the n-Si/TiO_2/NiO_x/pGr, n-Si/TiO_2/NiO_x/Gr, and n-Si/TiO_2/NiO_x photoanodes in the light (solid lines) compared to their corresponding p^+-Si/NiO_x/pGr, p^+-Si/NiO_x/Gr, and p^+-Si/NiO_x electrodes in the dark (dashed lines). (d) Typical Nyquist plots (with the equivalent circuit model) measured in 1 M KOH aqueous solution under AM 1.5G sunlight at 1.23 V_{RHE} for the n-Si/TiO_2/NiO_x/pGr, n-Si/TiO_2/NiO_x/Gr, and n-Si/TiO_2/NiO_x photoanodes.

2.3. Mechanism for improved OER performance

To elucidate the high PEC OER activity driver for the photoanodes with the pGr cover, both thermodynamics (photovoltage) and kinetics (reaction, charge and mass transfer) of the photoanodes were analyzed.[47,48] For thermodynamics, the photovoltage (V_{ph}) was calculated by comparing the voltage of the photoanodes under irradiation and that of the metallic p^+-Si system in the dark at the current of 10 mA cm^{-2}. The V_{ph} for the n-Si/TiO_2/NiO_x/pGr photoanode is presented in

Figure 5c with those of the n-Si/TiO_2/NiO_x/Gr and n-Si/TiO_2/NiO_x for comparison. For the three photoanodes, the n-Si/TiO_2/NiO_x/pGr with the best OER activity has the lowest V_{ph} of 382 mV, the worst n-Si/TiO_2/NiO_x/Gr shows the highest V_{ph} of 404 mV, and the V_{ph} of the cover-free control is 390 mV. This suggests that the enhanced PEC OER activity observed for the n-Si/TiO_2/NiO_x/pGr photoanode is primarily due to kinetic factors rather than the thermodynamic factor.

The kinetic overpotential required to produce a constant current of 10 mA cm^{-2} for the p^+-Si/NiO_x/pGr was calculated to be 390 mV, which is 120 and 30 mV lower than those for the p^+-Si/NiO_x/Gr (510 mV) and p^+-Si/NiO_x (420 mV), respectively (Figure S10, Supporting Information). Compared to the p^+-Si/NiO_x, the p^+-Si/NiO_x/pGr demonstrates superior OER kinetics and the p^+-Si/NiO_x/Gr is inferior, which is consistent with the above thermodynamic results.

PEC impedance spectroscopy measurements were further performed to explore the effect of the pGr cover on the charge transfer kinetics of the photoanodes in the PEC OER process. The Nyquist plots in Figure 5d consist of two semi-circles, which can be modeled using the equivalent circuit including the series resistance (R_S), charge transfer resistances in the photoanode (R_{int}) and at the photoanode/electrolyte interface (R_{CT}), and their corresponding constant phase angle elements (CPE_1 and CPE_2).[27] The fitted values of R_{CT} (Table S1, Supporting Information) reveal a considerable decrease in resistance for the n-Si/TiO_2/NiO_x/pGr (7.42 Ω cm^2) and a substantial increase for the n-Si/TiO_2/NiO_x/Gr (51.13 Ω cm^2) compared to that for the n-Si/TiO_2/NiO_x (10.76 Ω cm^2). This implies that the pGr cover promotes the charge injection kinetics of the NiO_x electrocatalyst, while the Gr cover reduces it, compared to that of the cover-free reference. Furthermore, to understand the charge separation in the n-Si/TiO_2/NiO_x/pGr photoanode, the barrier height at the n-Si surface was estimated by calculating the flat-band potential, as measured from Mott-Schottky plot (see Figure S11 for details, Supporting Information). Figure S11b displays the representative energy band diagram of the n-Si/TiO_2/NiO_x/pGr photoanode, which suggests that the photoholes generated in the n-Si can move easily to the surface NiO_x/pGr electrocatalyst through the TiO_2 tunneling layer. In contrast, photoelectrons from the n-Si to the NiO_x/pGr are restricted due to the high conduction band barrier (0.78 eV). Thus, the holes and electrons generated in the n-Si/TiO_2/NiO_x/pGr heterojunction can be readily separated and collected at the front and backside of the photoanode, respectively. Collectively, the results of the charge transfer and the above catalytic reaction kinetics corroborate that the PEC OER activity of the photoanode is ameliorated with the pGr cover through facilitating the kinetics while is weakened with the Gr cover out of its reduced kinetics. This highlights the salient role of the porous structure of the pGr cover in boosting the activity.

Additionally, we investigated the impact of the pGr cover on the mass transfer kinetics by assessing the stability of the photoanode structure, since a build-up of pressure from the gas product in the 2D covered catalytic microenvironment might induce structural damage and concomitant performance decrease. By examining the morphology of the photoanode after the PEC test, we found that the n-Si/TiO_2/NiO_x/pGr-15s with an optimal cover pore size maintains the integrity of the entire pGr sheet on the surface, indicating excellent structural stability (Figure S12a, Supporting Information). On the contrary, some ruptures with the size of about 1–2 µm were observable on the surface of the n-Si/TiO_2/NiO_x/pGr-5s photoanode owing to the formation of O_2 bubbles under the cover (Figure S12b, Supporting Information), and the intrinsic Gr layer almost completely peels off, leaving only a few residual Gr pieces on the surface of the n-Si/TiO_2/NiO_x/Gr sample (Figure S12c, Supporting Information).

The Gr cover is impermeable to gas and liquid, so it hinders the interfacial mass charge transfer kinetics between the photoanode surface and the electrolyte, ultimately leading to structural instability.[17,19] In contrast, the porous structure in the pGr cover with suitable pore size could provide channels for the diffusion of O_2 and electrolyte. As in the case of the n-Si/TiO_2/NiO_x/pGr-15s photoanode, the pores with the average size of 3.56 nm are large enough to allow for the release of O_2 bubbles and the diffusion of the electrolyte. Thus, the n-Si/TiO_2/NiO_x/pGr-15s photoanode and the photoanodes with longer bombardment time have good structure stability.

The influence of the cover pore size on the intrinsic activity of the pGr-covered NiO_x electrocatalyst in the n-Si/TiO_2/NiO_x/pGr photoanode is another important aspect to consider, which is addressed with DFT calculations. First, models were built to represent the NiO_x. According to our experimental observation (Figure S13, Supporting Information) and previous reports,[49] the active species of the NiO_x during the OER process is the NiOOH with layered structure. The hydroxylated surface has a higher catalytic activity than the stoichiometric one with half of the surface oxygen atoms hydroxylated. Thus, a hydroxylated NiOOH slab was built to represent the NiO_x (M), as shown in **Figure 6**a. Next, the pristine Gr covered system (Gr, Figure 6b) and those covered by the pGr with small pore sizes were built, i.e., the C1 (pGr/C1, Figure 6c) and C4 (pGr/C4, Figure 6d) vacancies with corresponding single- and four-carbon atom vacancy, respectively. In addition, the edge models with the zigzag (pGr/ZZ, Figure 6e) and armchair (pGr/AC, Figure 6f) configurations were adopted to represent the pGr with larger pore sizes. The dangling bonds at the edges are highly reactive under the OER condition, and thus the oxidation of the edges should be carefully evaluated. According to the Pourbaix diagram,[50] the Gr edge can be oxidized to the carbonyl group under our experimental condition. This is also in accordance with the observed percentage increase of C=O and C−O bonding in the pGr cover by the XPS analysis. The effect of the carbonyl group on the zigzag edge (pGr/O, Figure 6g) was also studied.

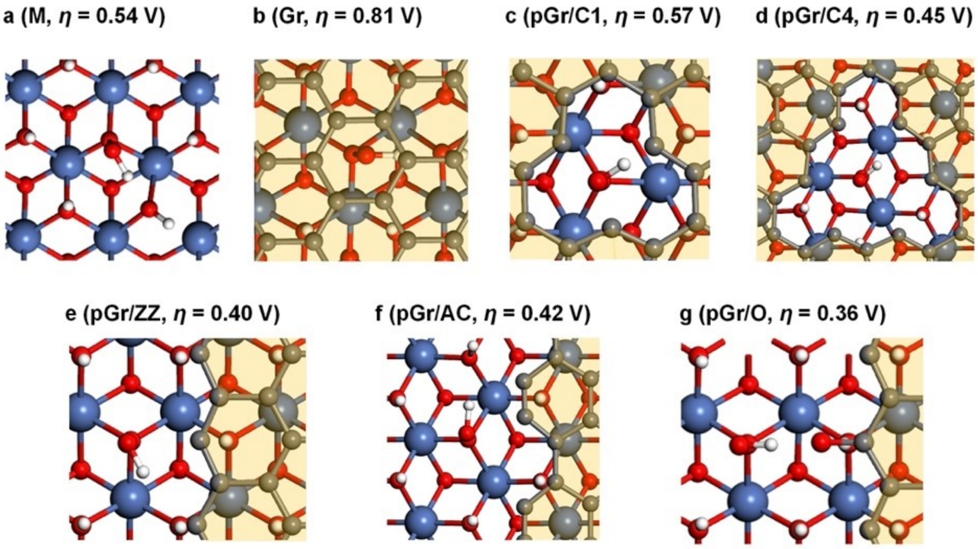

Figure 6. Top view of the constructed models and DFT calculated overpotentials for the (a) bare NiOOH and NiOOH covered by (b) pristine Gr, (c) pGr with C1 vacancy, (d) pGr with C4 vacancy, (e) pGr with zigzag edge, (f) pGr with armchair edge, (g) pGr with oxidized zigzag edge. The red, blue, white, and gray spheres represent the oxygen, nickel, hydrogen, and carbon atoms, respectively. For clarity, only the topmost NiOOH and Gr layers are shown, and the shade depicts the covered NiOOH by Gr.

The OER process in an alkaline environment follows the mechanism below:

$* + OH^- = *OH + e^-$ (R1)

$*OH + OH^- = *O + H_2O + e^-$ (R2)

$*O + OH^- = *OOH + e^-$ (R3)

$*OOH + OH^- = *O_2 + H_2O + e^-$ (R4)

$*O_2 = * + O_2$ (R5)

where * indicates the adsorbed species. The active sites for all the investigated systems are located on the NiOOH, and the potential limiting step is R3 which generates *OOH species. The DFT calculated overpotentials (η) are shown in Figure 6. The uncovered NiOOH has an overpotential of 0.54 V, and the coverage of the pristine Gr increases the overpotential to as high as 0.81 V. That is, besides the hindered accessibility for reactants, the higher overpotential also results in the decreased OER activity of the n-Si/TiO_2/NiO_x/Gr as compared to the n-Si/TiO_2/NiO_x photoanode. Then, the catalytic activities of the sites adjacent to the defects in various pGr-covered NiOOH models are further investigated. The C1 defect (Figure 6c) exhibits a higher η of 0.57 V than the uncovered system and will be incorporated by the generated O_2, blocking further reactions. But, all the other pore sizes are predicted to improve the OER activity over the bare NiOOH. The undercoordinated carbon atoms at the defective sites interact with adsorbed O and OOH species, stabilizing the intermediates and reducing the overpotential. With the enlargement of the pore sizes from the C1 and C4 vacancy to larger pores presented by the edge models, an increment in the OER activity is suggested with decreased overpotentials. This theoretical OER activity trend with increasing pGr pore sizes is well consistent with our experimental OER activity trend that has been observed with the increase of the pGr pore size from the n-Si/TiO_2/NiO_x/pGr-5s to the n-Si/TiO_2/NiO_x/pGr-15s photoanode. Moreover, when the pore edges are oxidized and form C=O groups as in our case, the hydrogen atoms in the *OOH groups form hydrogen bonds with the oxygen atoms in the C=O groups, which further stabilizes the structure, leading to an even lower overpotential of 0.36 V (Figure 6g). Consequently, these phenomena reveal that the pGr edges are key in enhancing the OER activity.

Meanwhile, the OER activity also depends on the total number of reactive sites near these pores. Much larger pores in the pGr sheet produced by excessive plasma bombardment severely decrease the specific surface area of the pGr, thus in turn reducing the active sites available for the OER process. Consequently, the OER activity of the n-Si/TiO_2/NiO_x/pGr photoanode exposed for longer bombardment time will drop due to the reason of the reduced number of active sites, albeit the charge and mass transfer are no longer the limiting step, as demonstrated by the photoanodes with the bombardment time longer than 15 s in our experimental observations.

Note that the common confinement effect in Gr-covered catalysts was not observed in our theoretical calculations. In our metal-OOH system with the Gr cover, the Coulombic interaction between the Gr cover and the underlying NiOOH surface appears to be insufficiently strong to substantially modify the electronic structure of the catalytic surface, although their distance of 2.85 Å is smaller than those (> 3.3 Å) of the previously reported 2D-covered metal or metal oxide catalysts and the Coulombic interaction in confined catalysis was reported to be central in tailoring the catalytic activity.[1,7,8,11] Therefore, the Gr cover has no obvious positive impact on the adsorption energies and energy barriers of the adsorbates on the NiOOH surface in our case,[1] and thus decreases the PEC OER activity compared to both the pGr-covered and cover-free photoanodes. In addition, we found that the PEC performance of our photoanode is comparable to most of the reported ones with noble-metal-free Ni-based electrocatalysts (Table S3). Notably, our investigation shows that the photoanode with the pGr cover yields a significant (twofold) improvement in photocurrent density at 1.23 V_{RHE} compared to the control sample without the cover. As a demonstration for further improvement in PEC activity, we fabricated a photoanode with the structure of n-Si/TiO_2/$NiFeO_x$/pGr, considering the better OER activity of $NiFeO_x$ compared to that of NiO_x. As shown in Figure S14, compared to the n-Si/TiO_2/$NiFeO_x$ photoanode, the onset potential of n-Si/TiO_2/$NiFeO_x$/pGr shifts from 1.07 to 1.02 V_{RHE} and its photocurrent at 1.23 V_{RHE} increases from 7.1 to 10.4 mA cm^{-2}, which is of the same order of magnitude as the best reported n-Si-based photoanodes. By carefully selecting or designing the more efficient tunneling layer (e.g., replacing TiO_2 with Al_2O_3 or ZrO_2), electrocatalyst layer (e.g., replacing NiO_x with Au/$NiFeO_x$), and/or 2D cover material, the PEC OER performance could be further improved using our porous cover strategy.

3. Conclusion

In summary, we have designed a 2D porous Gr cover structure to enhance the OER performance of the n-Si-based NiO_x photoanodes. We find that the pGr cover outperforms the Gr cover, which actually hinders the performance of the underlying catalyst. The enhanced performance of pGr is attributed to the effective charge and mass transfer between the photoanode and the electrolyte facilitated by the pores in pGr. These pores allow both charges and reactants to access the catalyst surface and enable effective release of produced O_2 from the surface. As a result, pGr ensures excellent activity and structural stability of the photoanodes during the PEC OER process. Further DFT calculations reveal that the pore edges with optimal sizes stabilize the adjacent reaction intermediates, enhancing intrinsic OER activity by reducing the catalytic overpotential. Our design highlights the critical role of the 2D porous cover structure in PEC water oxidation, which offers essential insights for catalyst design.

4. Experimental Section

Materials: The moderately phosphorous-doped n-type crystalline Si (100) wafers with a thickness of 500 ± 10 μm and a resistivity of 0.1−0.9 Ω cm (n-Si) were purchased from Zhejiang Lijing Guangdian Technology Co., Ltd. Single-layer graphene (Gr) with a coverage of > 99% on a 25 μm thick copper foil was supplied by Chongqing Graphene Technology Co., Ltd and SixCarbon Technology (Shenzhen). Metallic Ni wires (99.9%) were purchased from Zhongnuo New Material Co., Ltd.

Preparation of photoanodes: Five steps are involved in the sample preparation. First, n-Si wafers were cut into approximately 1 cm × 1 cm pieces and cleaned sequentially in an ultrasonic bath of acetone, isopropanol, and ethanol. Next, the pieces were immersed in a 2% HF solution for 2 min to remove the native oxide layer, followed by rinsing with deionized water and drying with flowing N_2 (step 1). A 2 nm thick passivation tunneling TiO_2 layer was deposited immediately on the n-Si substrates using atomic layer deposition (ALD) (step 2). Then, a 4 nm thick metallic Ni thin film was thermally evaporated onto the TiO_2 layer (step 3). A Gr layer was transferred onto the substrate using a poly(methyl methacrylate) (PMMA) assisted method (step 4). The sample was subsequently exposed to Ar plasma in a plasma cleaner instrument (CPC-A, CIF China) for 15 s and baked at ambient conditions for 10 min at 400 °C to obtain the n-Si/TiO_2/NiO_x/pGr photoanode (step 5). For comparison, the n-Si/TiO_2/NiO_x/Gr photoanode without the Ar plasma bombardment was obtained, and an analogous process was used to fabricate the cover-free n-Si/TiO_2/NiO_x photoanode. The same NiO_x/pGr, NiO_x/Gr, and NiO_x structures were also deposited on the p^+-Si substrate to examine their electrochemical properties.

To prepare electrodes for PEC measurements, the ohmic contacts was done on the backside of the n-Si samples by scratching the surface with a diamond scriber to remove the oxide layer, followed by cleaning the residue using ethanol; next, a droplet of InGa alloy was applied on the scratched surface, and a Cu wire was attached to it. Finally, the backside and frontside of the surface except for an active area of approximately 0.1-0.2 cm^2 were shielded by black 704 silicone rubber. Calibrated digital images and ImageJ software were employed to determine the exact geometric area of the active electrode surface.

ALD of TiO_2: The TiO_2 layer was deposited at a temperature of 200 °C using successive pulses of tetrakis (dimethylamido) titanium (70 °C) and H_2O (room temperature) as the titanium source and oxidant, respectively. The deposition was carried out under a N_2 carrier gas in a vacuum chamber using an ALD system (TALD-100A, KE-MICRO). In a typical process, one ALD cycle consists of tetrakis (dimethylamido) titanium dose for 0.2 s, N_2 purge for 40 s, H_2O dose for 0.2 s, and N_2 purge for 40 s. The growth rate of the TiO_2 layer was determined to be 0.04 nm per cycle using spectroscopic ellipsometry, and 60 cycles of ALD were performed to achieve a thickness of about 2.4 nm.

Thermal evaporation of Ni thin film: A thermal evaporator (ZHD-300, Techno) was used to prepare the Ni thin film. The base pressure of the vacuum chamber of this system was ~5×10^{-4} Pa. During the evaporation process, the current and voltage on a tungsten boat containing the Ni wire target were monitored to establish the vapor pressure in the chamber needed to maintain a constant evaporation rate of 1 Å s^{-1}. The film thickness was controlled using a quartz crystal thickness monitor.

PMMA assisted transfer of graphene: The copper (Cu) foil with Gr was cut into a suitable size (approximately 0.6 cm × 0.6 cm) and spin-coated with a PMMA solution (4 wt% dissolved in anisole) at 1000 rpm for 20 s, followed by 4000 rpm for 30 s. The resulting PMMA/Gr/Cu was cured at 120 °C for 2 min. Electrochemical delamination was then employed to remove the PMMA/Gr film from the Cu substrate by applying a cathode to anode dc voltage of 2 V in 1M NaOH electrolyte, with the PMMA/Gr/Cu as the cathode and a Pt foil as the anode. After separation from the Cu substrate, the resulting PMMA/Gr film was rinsed thoroughly with deionized water three times to eliminate any remaining etchant, and then placed on the target substrate to dry naturally. After baking at 120 °C for 10 min, the sample was immersed in an acetone bath for 1 h, followed by a warm acetone bath at 50 °C for 2 h, and then dipped into isopropyl alcohol for an additional 1 h to remove the PMMA film. Finally, the Gr-covered sample was obtained after drying with flowing N_2.

Characterizations: The morphology of the samples was evaluated using a Hitachi-SU8220 field emission scanning electron microscopy (SEM) at an accelerating voltage of 10 KV. Raman spectra were acquired using a Renishaw InVia Plus laser Raman spectrometer at room temperature with the 514 nm line of an Ar^+-ion laser as the excitation source. The Raman measurements were conducted at an incident laser power of around 1 mW to avoid graphene damage or laser-induced heating. X-ray photoelectron spectroscopy (XPS) was conducted with an ESCALAB250Xi using 300 W Al Kα radiation, and a base pressure of ~3×10^{-9} mbar was used. The binding energies were calibrated against the C 1s line at 284.8 eV from adventitious carbon. The acquired XPS spectra were analyzed with the XPSPEAK41 software, where a Shirley-type background was subtracted and the spectra were fitted with Gaussian-Lorentzian peaks with an 80% contribution of Gaussian character during peak deconvolution.

Photoelectrochemical measurements: All PEC measurements were carried out on a Zahner-Zennium electrochemical workstation at room temperature under a three-electrode configuration using a saturated calomel electrode (SCE) and a Pt foil as the reference electrode and the counter electrode, respectively. The as-prepared photoanodes were set as the working electrode, and a 1 M KOH aqueous solution (pH=13.62, measured by a pH meter) was employed as the electrolyte. A 500 W xenon lamp (Beijing Aulight Technology Co., Ltd.; CEL-S500) equipped with an AM 1.5G filter was used as the light source, and the light intensity was calibrated to be one sun (100 mW cm^{-2}) at the position of the photoanode using a fiber optic spectrometer (Avantes, Netherland; AvaSpec-ULS2048). All measured potentials were converted to the reversible hydrogen electrode (RHE) reference using the following equation: $V_{RHE} = V_{SCE} + 0.244\ V + 0.059pH$, where V_{SCE} is the measured potential against the SCE reference electrode. All reported potentials were intentionally not corrected by the ohmic drop (i.e., no *iR* correction). The photocurrent was recorded by linear sweep voltammetry with a scan rate of 20 mV s^{-1}. The PEC impedance spectroscopy (PEIS) was conducted under light irradiation conditions at 1.23 V_{RHE}, with an AC amplitude of 10 mV and a sweeping frequency range from 100 kHz to 0.1 Hz. Mott-Schottky measurements were performed in the dark using a Pt foil counter electrode and a Pt wire reference electrode in 50 mm $K_3Fe(CN)_6$, 350 mm $K_4Fe(CN)_6$, and 1 M KCl. During the measurement, the potential was swept from positive to negative values with a frequency of 7000 Hz and an AC amplitude of 5 mV. The stability data were obtained via chronoamperometry at the potential of 1.23 V_{RHE}. The amounts of evolved oxygen for the photoanode were determined by sampling aliquots (0.2 mL) in the headspace (50 mL) of the reactor to a gas chromatograph equipped with a molecular sieve 5 Å column and a TCD detector, in 1 M KOH electrolyte at 1.23 V_{RHE} under simulated solar irradiation. The Faradaic efficiency (FE) of photoanode was calculated using the following equation:

$$\mathrm{FE} = \frac{\text{Measured } \mathrm{O_2} \text{ evolution}}{\text{Calculated } \mathrm{O_2} \text{ evolution}} = \frac{\text{Measured } \mathrm{O_2} \text{ evolution}}{(\frac{J_{photo} \times T}{e}/4)/N_A} \times 100\% \qquad (1)$$

where J_{photo} is the photocurrent (A), T is the measurement time (sec), e is the charge magnitude of an electron (1.602 $\times 10^{-19}$ C), and N_A is Avogadro's constant (6.02×10^{23} mol^{-1}).

DFT calculations: DFT calculations were performed within the Vienna Ab-initio Simulation Package (VASP) package[51-54] with the Projected Augmented Waves (PAW) basis and Perdew-Burke-Ernzerhof (PBE)[55] exchange-correlation functional. Hubbard *U* correction was employed to describe the exchange interaction of Ni 3d orbitals. The effective *U* value of 5.5 eV was adopted according to the reference.[49] Spin-polarized calculations were performed with the Grimme's DFT-D2 method[56] accounting for van der Waals interaction. The structure of the β-NiOOH (001) surface (M) was adopted from Tkalych et al.'s work[49] with four layers of $\sqrt{3} \times \sqrt{3}$ surface supercell on the basis of the reference. Graphene was overlaid above the slab to represent the pristine graphene-covered NiOOH system (Gr). The 4 × 4 graphene supercell was chosen to fit the lattice parameter of the NiOOH, with the lattice mismatch of only 3.55 %. A point defect model (pGr/C1) was built on the basis of the perfect graphene-covered slab. Given the system size and computational cost, a larger surface model of $2\sqrt{3}\times2\sqrt{3}$ supercell with three layers was constructed to reveal the influence of a C4 vacancy on the OER procedure (pGr/C4). A $2\sqrt{3}\times\sqrt{3}$ surface supercell was built to examine the catalytic process of the NiOOH adjacent to the graphene edge. The bottom layer was fixed. The zigzag (pGr/ZZ) and armchair edge (pGr/AC) configurations were considered. In addition, the oxidized graphene with a carbonyl group attached to the edge was built according to the pourbaix diagram of graphene (pGr/O).

The geometries for the OER intermediates of the above-mentioned systems were optimized while the bottom two layers of the NiOOH slab were fixed. The 400 eV energy cutoff was adopted. Gamma-centered k-point mesh of 3×3×1 was adopted in the calculation of M, Gr and pGr/C1 systems. A 3×1×1 k-point was applied to the edge models of pGr/ZZ, pGr/AC and pGr/O. Gamma point only calculation was performed for the large pGr/C4 model. The energetics were further refined with an energy cutoff of 600 eV. The solvation effect of water was considered using the VASPsol module during the energy refinement. The reaction Gibbs free energies (ΔG) were determined through the equation of $\Delta G = \Delta E - T\Delta S + \Delta ZPE$, where ΔE is the reaction energy. T, ΔS and ΔZPE are the thermal correction part which stands for temperature, entropy change and zero-point energy change, respectively. All the thermal correction data adopted in this article were from the reference. Of note, the Gibbs free energy for the O_2 molecule was determined with $G_{O2} = 4.92 + 2G_{H2O} - 2G_{H2}$. The predicted energies were listed in Supplementary Table S2.

Supporting Information

Supporting Information is available from the Wiley Online Library or from the author.

Acknowledgements

G. Xie and X. Liu contributed equally to this work. The authors acknowledge financial support for this work from the Strategic Priority Research Program of CAS (XDB36000000), and the National Natural Science Foundation of China (22102037, 22179028, 22002028).

Received: ((will be filled in by the editorial staff))
Revised: ((will be filled in by the editorial staff))
Published online: ((will be filled in by the editorial staff))

References

[1] T. A. Shifa, A. Vomiero, *Adv. Energy Mater.* **2019,** *9*, 1902307.

[2] H. Li, J. Xiao, Q. Fu, X. Bao, *Proc. Natl. Acad. Sci.* **2017,** *114*, 5930-5934.

[3] Y. Yao, Q. Fu, Y. Zhang, X. Weng, H. Li, M. Chen, L. Jin, A. Dong, R. Mu, P. Jiang, *Proc. Natl. Acad. Sci.* **2014,** *111*, 17023-17028.

[4] S. H. Petrosko, R. Johnson, H. White, C. A. Mirkin, *J. Am. Chem. Soc.* **2016,** *138*, 7443-7445.

[5] Y. Zhang, X. Weng, H. Li, H. Li, M. Wei, J. Xiao, Z. Liu, M. Chen, Q. Fu, X. Bao, *Nano Lett.* **2015,** *15*, 3616-3623.

[6] Y. Zhou, W. Chen, P. Cui, J. Zeng, Z. Lin, E. Kaxiras, Z. Zhang, *Nano Lett.* **2016,** *16*, 6058-6063.

[7] H. Li, C. Guo, Q. Fu, J. Xiao, *J. Phys. Chem. Lett.* **2019,** *10*, 533-539.

[8] Z. Z. Lin, X. Chen, C. Yin, L. Yue, F. X. Meng, *Int. J. Energy Res.* **2020,** *44*, 784-794.

[9] X. Chen, Z.-Z. Lin, M. Ju, L.-X. Guo, *Appl. Surf. Sci.* **2019,** *479*, 685-692.

[10] S. Wang, Y. Feng, M. a. Yu, Q. Wan, S. Lin, *ACS Appl. Mater. Interfaces* **2017,** *9*, 33267-33273.

[11] F. Wei, Q. Wan, S. Lin, H. Guo, *J. Phys. Chem. C* **2020**.

[12] P. Sun, Q. Yang, W. Kuang, Y. Stebunov, W. Xiong, J. Yu, R. R. Nair, M. Katsnelson, S. Yuan, I. Grigorieva, *Nature* **2020,** *579*, 229-232.

[13] Y. Fu, A. V. Rudnev, G. K. Wiberg, M. Arenz, *Angew. Chem. Int. Ed.* **2017,** *56*, 12883-12887.

[14] N. Arulmozhi, S. Hanselman, V. Tudor, X. Chen, D. van Velden, G. F. Schneider, F. Calle-Vallejo, M. T. M. Koper, *JACS Au* **2023,** *3*, 526-535.

[15] X. Cui, P. Ren, C. Ma, J. Zhao, R. Chen, S. Chen, N. P. Rajan, H. Li, L. Yu, Z. Tian, *Adv. Mater.* **2020,** *32*, 1908126.

[16] S. Gong, C. Wang, P. Jiang, K. Yang, J. Lu, M. Huang, S. Chen, J. Wang, Q. Chen, *J. Mater. Chem. A* **2019,** *7*, 15079-15088.

[17] K. Hu, T. Ohto, Y. Nagata, M. Wakisaka, Y. Aoki, J.-i. Fujita, Y. Ito, *Nat. Commun.* **2021,** *12*, 203.

[18] T. Kosmala, A. Baby, M. Lunardon, D. Perilli, H. Liu, C. Durante, C. Di Valentin, S. Agnoli, G. Granozzi, *Nat. Catal.* **2021,** *4*, 850-859.

[19] A. J. Shih, N. Arulmozhi, M. T. Koper, *ACS Catal.* **2021,** *11*, 10892-10901.

[20] K. Sun, F. H. Saadi, M. F. Lichterman, W. G. Hale, H.-P. Wang, X. Zhou, N. T. Plymale, S. T. Omelchenko, J.-H. He, K. M. Papadantonakis, *Proc. Natl. Acad. Sci.* **2015,** *112*, 3612-3617.

[21] X. Zhou, R. Liu, K. Sun, D. Friedrich, M. T. McDowell, F. Yang, S. T. Omelchenko, F. H. Saadi, A. C. Nielander, S. Yalamanchili, *Energy Environ. Sci.* **2015,** *8*, 2644-2649.

[22] I. A. Digdaya, G. W. P. Adhyaksa, B. J. Trześniewski, E. C. Garnett, W. A. Smith, *Nat. Commun.* **2017,** *8*, 15968.

[23] A. C. Ferrari, D. M. Basko, *Nat. Nanotechnol.* **2013,** *8*, 235-246.

[24] L. Malard, M. Pimenta, G. Dresselhaus, M. Dresselhaus, *Phys. Rep.* **2009,** *473*, 51-87.

[25] S. A. Lee, T. H. Lee, C. Kim, M. G. Lee, M.-J. Choi, H. Park, S. Choi, J. Oh, H. W. Jang, *ACS Catal.* **2018,** *8*, 7261-7269.

[26] B. Guo, A. Batool, G. Xie, R. Boddula, L. Tian, S. U. Jan, J. R. Gong, *Nano Lett.* **2018,** *18*, 1516-1521.

[27] C. Li, M. Huang, Y. Zhong, L. Zhang, Y. Xiao, H. Zhu, *Chem. Mater.* **2019,** *31*, 171-178.

[28] S. Chen, L. Brown, M. Levendorf, W. Cai, S.-Y. Ju, J. Edgeworth, X. Li, C. W. Magnuson, A. Velamakanni, R. D. Piner, *ACS Nano* **2011,** *5*, 1321-1327.

[29] M. Schriver, W. Regan, W. J. Gannett, A. M. Zaniewski, M. F. Crommie, A. Zettl, *ACS Nano* **2013,** *7*, 5763-5768.

[30] G. Zhu, W. Zhu, Y. Lou, J. Ma, W. Yao, R. Zong, Y. Zhu, *Nat. Commun.* **2021,** *12*, 4152.

[31] A. Kovtun, D. Jones, S. Dell'Elce, E. Treossi, A. Liscio, V. Palermo, *Carbon* **2019,** *143*, 268-275.

[32] N.-F. Chiu, C.-D. Yang, C.-C. Chen, C.-T. Kuo, *Sens. Actuators B Chem.* **2018,** *258*, 981-990.

[33] S. Riyajuddin, K. Azmi, M. Pahuja, S. Kumar, T. Maruyama, C. Bera, K. Ghosh, *ACS Nano* **2021,** *15*, 5586-5599.

[34] F. Tang, W. Cheng, Y. Huang, H. Su, T. Yao, Q. Liu, J. Liu, F. Hu, Y. Jiang, Z. Sun, *ACS Appl. Mater. Interfaces* **2017,** *9*, 26867-26873.

[35] L. G. Cançado, A. Jorio, E. M. Ferreira, F. Stavale, C. A. Achete, R. B. Capaz, M. V. d. O. Moutinho, A. Lombardo, T. Kulmala, A. C. Ferrari, *Nano Lett.* **2011,** *11*, 3190-3196.

[36] A. Eckmann, A. Felten, I. Verzhbitskiy, R. Davey, C. Casiraghi, *Phys. Rev. B* **2013,** *88*, 035426.

[37] B. Guo, Q. Liu, E. Chen, H. Zhu, L. Fang, J. R. Gong, *Nano Lett.* **2010,** *10*, 4975-4980.

[38] L. Gao, W. Ren, B. Liu, R. Saito, Z.-S. Wu, S. Li, C. Jiang, F. Li, H.-M. Cheng, *ACS Nano* **2009,** *3*, 933-939.

[39] M. Iqbal, O. Kelekci, M. Iqbal, J. Eom, *Carbon* **2013,** *59*, 366-371.

[40] W. Guo, S. M. Mahurin, R. R. Unocic, H. Luo, S. Dai, *Nano Lett.* **2020,** *20*, 7995-8000.

[41] M. M. Lucchese, F. Stavale, E. M. Ferreira, C. Vilani, M. V. d. O. Moutinho, R. B. Capaz, C. A. Achete, A. Jorio, *Carbon* **2010,** *48*, 1592-1597.

[42] A. Eckmann, A. Felten, A. Mishchenko, L. Britnell, R. Krupke, K. S. Novoselov, C. Casiraghi, *Nano Lett.* **2012,** *12*, 3925-3930.

[43] J. Zhao, G. He, S. Huang, L. Villalobos, M. Dakhchoune, H. Bassas, K. Agrawal, *Sci. Adv.* **2019,** *5*, eaav1851.

[44] C.-T. Pan, J. Hinks, Q. M. Ramasse, G. Greaves, U. Bangert, S. Donnelly, S. Haigh, *Sci. Rep.* **2014,** *4*, 1-7.

[45] A. C. Ferrari, J. Robertson, *Phys. Rev. B* **2000,** *61*, 14095.

[46] S. Lee, L. Ji, A. C. De Palma, E. T. Yu, *Nat. Commun.* **2021,** *12*, 3982.

[47] J. E. Thorne, S. Li, C. Du, G. Qin, D. Wang, *J. Phys. Chem. Lett.* **2015,** *6*, 4083-4088.

[48] Y. Dai, J. Yu, C. Cheng, P. Tan, M. Ni, *J. Mater. Chem. A* **2020,** *8*, 6984-7002.

[49] A. J. Tkalych, H. L. Zhuang, E. A. Carter, *ACS Catal.* **2017,** *7*, 5329-5339.

[50] D. San Roman, D. Krishnamurthy, R. Garg, H. Hafiz, M. Lamparski, N. T. Nuhfer, V. Meunier, V. Viswanathan, T. Cohen-Karni, *ACS Catal.* **2020,** *10*, 1993-2008.

[51] G. Kresse, J. Furthmüller, *Comput. Mater. Sci.* **1996,** *6*, 15-50.

[52] G. Kresse, J. Hafner, *Phys. Rev. B* **1994,** *49*, 14251.

[53] G. Kresse, J. Hafner, *Phys. Rev. B* **1993,** *47*, 558.

[54] G. Kresse, J. Furthmüller, *Phys. Rev. B* **1996,** *54*, 11169.

[55] J. P. Perdew, K. Burke, M. Ernzerhof, *Phys. Rev. Lett.* **1996,** *77*, 3865.

[56] S. Grimme, *J. Comput. Chem* **2006,** *27*, 1787-1799.

A porous graphene (pGr)-covered NiO_x electrocatalyst is designed to improve water oxidation of Si-based photoanodes, compared to the intrinsic Gr cover and cover-free counterparts. It demonstrates the pGr cover with optimized pore size balances the interfacial charge and mass transfer, ensures the structural stability of photoanodes, and enhances the intrinsic catalytic activity of active sites by reducing the reaction overpotential.

G. X., X. L., B.G., T. T.,* J. R. G.*

Porous 2D Catalyst Covers Improve Photoelectrochemical Water-oxidation Performance